Nonlinear Multiscale Analysis of 3D Echocardiographic Sequences

Alessandro Sarti, Karol Mikula, Fiorella Sgallari

Abstract

We introduce a new model for multiscale analysis of space-time echocardiographic sequences. The proposed nonlinear partial differential equation, representing the multiscale analysis, filters the sequence with keeping of the space-time coherent structures. It combines the ideas of regularized Perona-Malik anisotropic diffusion and Galilean invariant movie multiscale analysis of Alvarez, Guichard, Lions and Morel. The numerical method for solving the proposed partial differential equation is suggested and its stability is shown. The computational results are discussed.

Keywords

Echocardiography, image multiscale analysis, nonlinear scale space, partial differential equations, numerical solution

I. Introduction

Two-dimensional (2D) echocardiography is currently an imaging modality most frequently used in cardiology due to its simplicity, lack of ionizing radiation and a relative low cost. However, 2D echocardiography allows visualization of only tomographic planar sections of the heart; thus to obtain a complete evaluation of the heart anatomy and function, the physician must reassemble mentally a three-dimensional (3D) model from multiple two-dimensional images. Moreover, 2D echocardiography relies on geometrical assumptions for the determination of heart chamber volumes and thus presents a considerable measurement error, especially for the right ventricular and atrial volume determination ([5]). 3D echocardiography may avoid the need for geometrical assumptions, thereby allowing accurate evaluation of chambers size and shape, even in the case of cavities with irregular or distorted geometry. The correct visualization and interpretation of 3D echo images is often affected by the high amount of noise intrinsically linked to the acquisition method. It is absolutely necessary to submit the data to pre-processing in order to improve their legibility from a clinical point of view. The application of traditional pre-processing algorithms (moving average, median and Gaussian filtering) does not reduce the noise superimposed to the image maintaining a good definition of the interfaces ([15]). Nonlinear filtering methods based on partial differential equations have been applied in [22], [11] to 3D echocardiographic images (however, without considering a time coherence of successive echocardiographic frames). The importance of noise removal by nonlinear filtering both for visualization purposes as well as optical flow estimation has been also outlined by several authors (see e.g. [3], [19]). The processing algorithm should be able to distinguish the noise from the contours of the different cardiac structures by using both spatial and temporal coherence.

In order to follow these aims we use the approach based on the so called image multiscale analysis, i.e. the application of a special nonlinear partial differential equation (PDE) to an initial image. We propose a nonlinear PDE, representing the multiscale analysis, which combines ideas of the regularized Perona-Malik anisotropic diffusion model and Galilean invariant movie multiscale analysis equation of Alvarez, Guichard, Lions and Morel. It filters the space-time image sequence with respecting of the spatial as well as temporal coherent structures. The semi-implicit in scale, linear and unconditionally stable numerical method is proposed for solving the problem in discrete form. The space discretization is based on finite volume technique, which is widely used in the computational community dealing with numerical methods for diffusion equations. The

Alessandro Sarti is with the Department of Mathematics of University of California at Berkeley and of Lawrence Berkeley National Laboratory, Berkeley, USA, Karol Mikula is with Department of Mathematics, Slovak University of Technology, Bratislava, Slovakia and Fiorella Sgallari is with Department of Mathematics, University of Bologna, Italy

proposed approximation leads to solving of a linear system of equations for each frame of the sequence in each discrete scale step. It can be done efficiently using standard or parallel methods of linear algebra.

The rest of the paper is organized as follows: in section II we introduce the main equation and we outline its general features. In section III we describe an approximation scheme and a numerical method to solve the non-linear multiscale analysis for 3D sequences. In section IV we present the results obtained by applying the filtering to a synthetic image sequence and to a real 3D echocardiographic sequence. The qualitative and quantitative assessment of the accuracy of the results are provided. In section V we explain why 3D ultrasound sequences fulfill the requirements of our multiscale analysis model. The last part of the section will deal with a comparison among several linear solvers for discrete equations. Conclusions are presented in section VI.

II. The model equation

The input echocardiographic sequence can be modelled by a real function $u_0(x_1, x_2, x_3, \theta)$, $u_0 : \Omega \times [0, T] \to I\!R$, where $\Omega \subset I\!R^N$ represents a spatial domain and $[0, T]$ is the time interval in which the acquisition is performed. In practice, Ω is a rectangular domain and $N = 2$ for 2D echocardiography or $N = 3$ for 3D echocardiography. The time sequence can be periodically prolonged from $[0, T]$ to $I\!R$. The typical example which can be represented by such u_0 is an ultrasound acquisition of an entire cardiac cycle.

The image multiscale analysis, as it has been introduced in [1], associates with u_0 a family $u(t, x_1, x_2, x_3, \theta)$ of smoothed - simplified images (in our case a family of smoothed - filtered sequences) depending on an abstract parameter t, the *scale*. As it has been proved in [1], if such family fulfills basic assumptions - pyramidal structure, regularity and local comparison principle - then, it can be represented as a (viscosity in the sense of [7]) solution of a second order (degenerate) parabolic partial differential equation

$$\frac{\partial u}{\partial t} = F(t, u, Du, D^2u) \tag{1}$$

with the initial condition given by

$$u(0, x_1, x_2, x_3, \theta) = u_0(x_1, x_2, x_3, \theta). \tag{2}$$

In (1) and in the sequel, we denote the vector of first partial derivatives with respect to all space and time variables x_1, x_2, x_3, θ by Du, while ∇u denotes its spatial part. D^2u is the matrix of second order derivatives with respect of all space and time variables.

The echocardiographic space-time sequence is a 4D image and we can apply (1)-(2) to it. The question is how to choose the right hand side of (1) in order to extract the most important information from the sequence, filter out the noise and enhance relevant moving structures. First we will write the continuous model and in the next chapter its discrete-numerical analogy.

We will assume that certain objects acquired in different time, and thus being in different frames of the sequence, are formed by points that preserve their intensity along the motion trajectory. Such objects are called Lambertian structures. Moreover we assume that motion is Galilean locally in time, i.e. the motion trajectories are smooth in time. Designing the model we consider the following quantity (see [1], [2]) proposed by Guichard ([10])

$$\begin{aligned} clt(u) = \min_{w_1, w_2} \frac{1}{(\Delta\theta)^2} (&| < \nabla u, w_1 - w_2 > | + \\ &|u(x - w_1, \theta - \Delta\theta) - u(x, \theta)| + \\ &|u(x + w_2, \theta + \Delta\theta) - u(x, \theta)|) \end{aligned} \tag{3}$$

where w_1, w_2 are arbitrary vectors in $I\!R^N$ and $\Delta\theta$ is the time increment. The scalar function $clt(u)$ (the name clt indicates the relation to the curvature of Lambertian trajectory) will introduce a measure of coherence in time for the moving structures. It consists of the sum of three positive parts and we want to find the minimum in all possible directions w_1, w_2. The last two terms in the sum on the right hand side of (3) are related to the differences in the intensities of end-points of candidate Lambertian velocity vectors w_1, w_2. To find the

directions of such vectors we look at the points which have the closest intensity value to the intensity $u(x,\theta)$ in the previous frame (term $|u(x-w_1,\theta-\Delta\theta)-u(x,\theta)|$) and in the next frame (term $|u(x+w_2,\theta+\Delta\theta)-u(x,\theta)|$). Those differences are scaled by the factor $1/(\Delta\theta)^2$. Note that, if we find corresponding Lambertian points both terms vanish. The first term in the sum, namely $|<\nabla u, w_1-w_2>|/(\Delta\theta)^2$, corresponds to the so called *apparent acceleration*, i.e. to the difference between candidate Lambertian velocity vectors w_1 and w_2 in the direction of ∇u. For details and some more background from the optical flow point of view we refer to [1], [2], [10]. The quantity $clt(u)$ is thus related to the curvature of the space-time level curve passing through the space-time point (x,θ), i.e. to the curvature of Lambertian trajectory. The value of $clt(u)$ vanishes for the Lambertian points that are in Galilean motion. It is consistent with our purposes to not alter such trajectories. On the other hand for the noisy points there is no motion coherence and thus $clt(u)$ will be large there.

Concerning the space coherence, we assume that distinguished structures are located in the regions with a certain mean value of the image intensity function and that object boundary forms an edge in the image. On the edges, the gradient of image is large. We intend to keep the object boundaries, thus we want to construct a diffusion process which will not blur or move the edges. It is clear, that such requirement will be fulfilled when the coefficient of spatial diffusion will be small on edges and large outside them. For that reason we have chosen the regularized Perona-Malik *anisotropic diffusion* introduced in [8] where the diffusion process is designed in such way.

To combine the benefits of both time and spatial coherence we propose the following PDE

$$\frac{\partial u}{\partial t} = clt(u)\nabla.(g(|\nabla G_\sigma * u|)\nabla u) \tag{4}$$

together with initial condition (2). We consider zero Neumann boundary conditions in the spatial part of the boundary and periodic boundary conditions in time. The parameters in (4) fulfill the following assumptions

$$\begin{aligned} &g \text{ is a continuous function,} \\ &g(0)=1 \text{ and } 0<g(s)\to 0 \text{ for } s\to\infty, \end{aligned} \tag{5}$$

$$\begin{aligned} &G_\sigma \in C^\infty(\mathbb{R}^N) \text{ is a smoothing kernel,} \\ &\int_{\mathbb{R}^N} G_\sigma(x)dx = 1, \\ &G_\sigma(x)\to\delta_x \text{ for } \sigma\to 0, \\ &\delta_x \text{ - the Dirac measure at point } x. \end{aligned} \tag{6}$$

Let us note that by the term $\nabla G_\sigma * u$ in (4) we mean $\int\limits_{\mathbb{R}^N} \nabla G_\sigma(x-\xi)\tilde{u}(\xi)d\xi$, where $\tilde{u}$ is an extension of u by reflection over the spatial boundaries. The possible choices of the two previous parameters are e.g.

$$g(s) = \frac{1}{1+K*s^2} \tag{7}$$

with some constant K ([26]), and N-dimensional Gauss function ([8])

$$G_\sigma(x) = \frac{1}{(2\sqrt{\pi\sigma})^N} e^{-\frac{|x|^2}{4\sigma}}. \tag{8}$$

Due to the shape of the function g (see general assumption (5) and the (usual) choice (7)), the spatial diffusion process is slowed down in the points where the *Gaussian gradient* $\nabla G_\sigma * u$ is large. In the regions with the small variation in the signal the smoothing is close to standard linear diffusion due to $g(0)=1$. In the original Perona-Malik model the diffusion depends simply on $|\nabla u|$. Introducing $|\nabla G_\sigma * u|$ instead of $|\nabla u|$ makes the process more stable with respect to noise and the model does not keep the so called 'spurious' edges ([8]). With G_σ given by (8), the convolution property $\nabla G_\sigma * u = G_\sigma * \nabla u = \nabla(G_\sigma * u)$ holds true. Thus the term $\nabla G_\sigma * u$ in (4) represents the smoothing of the spatial gradient, i.e. $G_\sigma * \nabla u$, and also the gradient

of the solution of the linear diffusion (heat) equation at the time σ with initial condition given by u, i.e. $\nabla(G_\sigma * u)$. We will use that fact also in our numerical implementation. The result of the convolution is used as the input for the function g. Thus one can consider the spatial Catté, Lions, Morel and Coll diffusion term $\nabla.(g(|\nabla G_\sigma * u|))$ as a coupling of nonlinear Perona-Malik diffusion and linear diffusion.

The change of image intensity in scale, i.e. $\frac{\partial u}{\partial t}$, is given by the right hand side of (4) where Perona-Malik term is multiplied by $clt(u)$. Thus, the diffusion process degenerates (is stopped) in the Lambertian points that are in Galilean motion. It is the important difference from standard (e.g. *anisotropic*) selective smoothing processes. We can conclude that, the equation (4) preserves moving in time structures as well as keeps their spatial edges. The features of the spatial nonlinear selective smoothing given by Perona-Malik term $\nabla.(g(|\nabla G_\sigma * u|))$ and of the Guichard's acceleration term $clt(u)$ are connected in our model equation (4).

Remark 1. The equation (4) is related to the 2D-movie multiscale analysis introduced by Alvarez, Guichard, Lions and Morel in [1] and by Guichard in [10]. If additional assumptions, namely time-translation, space-Euclidean and morphological invariance, are added to the basic hypotheses of image processing, then 2D-movie multiscale analysis obeys the PDE of the form

$$\frac{\partial u}{\partial t} = |\nabla u| F(t, curv(u), accel(u))$$

where *curv* refers to the mean curvature of spatial level sets of u and *accel* refers to the continuous apparent acceleration. Moreover, assuming space and time affine invariance, the only multiscale analysis has the form ([1])

$$\frac{\partial u}{\partial t} = (|\nabla u| curv(u)^{1/3})^{1-q}$$
$$((|\nabla u|(sgn(curv(u))accel(u))^+)^q$$

for $q \in [0,1]$, where *sgn* is the signum function and $()^+$ means positive part of real number. The special interesting case is $q = \frac{1}{4}$, when the previous equation reduces to

$$\frac{\partial u}{\partial t} = |Du|(G(u)^+)^{1/4}$$

where $G(u)$ is the Gaussian curvature of level surface in 3D space ([1], [2], [6]).

Remark 2. In the equation (4), we can consider $|\nabla u| curv(u) = |\nabla u| \nabla . \frac{\nabla u}{|\nabla u|}$ instead of the Perona-Malik type term $\nabla.(g(|\nabla G_\sigma * u|)\nabla u)$ for spatial smoothing process. Such model can be useful not for strict spatial edges keeping, but e.g. for slight smoothing of silhouettes of moving objects by multiscale analysis (see also [22]). The similar implementation ideas as described in the next section can be applied also for such *level-set type equation* ([23], [29], [30],[11], [22]).

III. Numerical scheme

In this section we describe a numerical solution method for the image sequence multiscale analysis represented by the equation (4). First let us give some useful notations. Let our space-time sequence consist of $m+1$ frames. Let $\vartheta = \frac{T}{m}$ be the discrete time step of the sequence. Let us denote a discrete scale step by τ. Then by u^i_j we denote the j-th frame of the sequence in the i-th discrete scale step, i.e.

$$u^i_j(x_1, x_2, x_3) = u(i\tau, x_1, x_2, x_3, j\vartheta). \tag{9}$$

The basic idea of our numerical approximation is to handle terms in (4) in such a way to obtain a linear boundary value problem for u^i_j. The reason is that, such equations can be solved by robust and efficient spatial discretization techniques based on finite volume (FVM), finite difference (FDM) or finite element methods (FEM). To that goal, the nonlinearities of equation (4) are treated using the previous scale step, while the linear terms are handled implicitly. Such approach is called semi-implicit approximation in scale ([34], [35], [12],[4],[11]). The term semi-implicit is related to the fact that the nonlinear parts of the equation are treated

from the previous step, like in the explicit method, while the linear ones are taken from the actual step, like in the implicit schemes. Then we provide space-time discretization and our numerical method leads to solving of linear algebraic system in order to update each frame in the sequence in the new scale. It is clear that the semi-implicit approach is robust, because it avoids the stability problems (see Appendix) arising in explicit schemes. At the same time we do not need to solve nonlinear algebraic systems as in fully-implicit schemes.

Let us discuss the discretization of the terms in (4) in details. From definition (3) we can obtain a time-discrete version of $clt(u)$ considering the current, previous and next time frame of the sequence. We define

$$\begin{aligned} clt(u_j^i) = \min_{w_1,w_2} \frac{1}{\vartheta^2}(| < \nabla u_j^i, w_1 - w_2 > | + \\ |u_{j-1}^i(x - w_1) - u_j^i(x)| + \\ |u_{j+1}^i(x + w_2) - u_j^i(x)|). \end{aligned} \tag{10}$$

Now, we can write the **semi-implicit scheme** for solving (4). Let τ be the given discrete scale step and σ be the given variance of the kernel. For $i = 1, 2, ...$ and for each frame $j = 0, ..., m$ we look for u_j^i satisfying

$$\frac{u_j^i - u_j^{i-1}}{\tau} = clt(u_j^{i-1}) \nabla .(g(|\nabla G_\sigma * u_j^{i-1}|) \nabla u_j^i) \tag{11}$$

where the periodicity of the sequence is used for $j = 0$ and $j = m$ and zero Neumann boundary conditions are considered for the spatial boundary Ω. We can use also other conditions to update the first and the last frame in the sequence (e.g. reflexive, if only one half of the cardiac cycle is given). The equation (11) for the unknown function u_j^i is elliptic PDE in points where $clt(u_j^{i-1}) > 0$ while it degenerates to the algebraic identity in points where $clt(u_j^{i-1}) = 0$.

We can use the convolution derivative property $\nabla G_\sigma * u_j^{i-1} = \nabla (G_\sigma * u_j^{i-1})$ and perform the convolution solving numerically the linear heat equation

$$\frac{\partial \varphi}{\partial t} = \nabla .(\nabla \varphi) \tag{12}$$

in the time interval $[0, \sigma]$ with the initial condition $\varphi(x, 0) = u_j^{i-1}(x)$. Then we take $u_j^\sigma = \varphi(x, \sigma)$ and $|\nabla u_j^\sigma|$ is used as the edge indicator. Numerically we solve the equation (12) implicitly in t with just one discrete scale step of length σ. Thus, the scheme (11) can be rewritten into the couple of semi-discrete linear equations

$$\frac{u_j^i - u_j^{i-1}}{\tau} = clt(u_j^{i-1}) \nabla .(g(|\nabla u_j^\sigma|) \nabla u_j^i) \tag{13}$$

where u_j^σ is the solution of

$$\frac{u_j^\sigma - u_j^{i-1}}{\sigma} = \nabla .(\nabla u_j^\sigma) \tag{14}$$

$$j = 0, ..., m, \quad i = 1, 2, ... \tag{15}$$

Now we will discuss the discretization of (13)-(14) on a given spatial discrete pixels/voxels structure. In discrete settings, $\min\limits_{w_1,w_2}$ in (10) is evaluated only for vectors connecting pixels/voxels centers denoted by P (see also [10]). We look only to a certain rectangular neighborhood centered in P.

For space discretization of (13) as well as (14) we use the so called finite (or control) volume method. This method is widely used in engineering and applied mathematics community for numerical computations of diffusion (convection-diffusion and conservation laws as well) processes ([24]). In such approach, 3D space is divided into a set of finite volumes and the partial differential equation is approximated by balancing the flux through the finite volume boundaries. Let the discrete image intensity values be given in the central

points P of finite volumes corresponding to voxels in 3D. Let h denote the distance between two such points (we consider uniform 3D grid in this explanation, but all considerations can be generalized to nonuniform, non-rectangular 2D or 3D grids). Let us denote the grid neighbors of P by W (west), E (east), S (south), N (north), B (bottom), U (up) and the central points of the faces of the finite in direction of neighbors by w, e, s, n, b, u. The finite volume around P then can be written as $\mathcal{V} = [w,e] \times [s,n] \times [b,u] \subset I\!R^3$.

To simplify the notation, denote $d \equiv g(|\nabla u_j^\sigma|)$. Let us integrate the equation (13) in the finite volume $\mathcal{V}$. We obtain

$$\begin{aligned}
&\int_w^e \int_s^n \int_b^u u_j^i dx_1 dx_2 dx_3 = \\
&\tau \int_w^e \int_s^n \int_b^u clt(u_j^{i-1})(\frac{\partial}{\partial x_1}(d\frac{\partial u_j^i}{\partial x_1}) + \\
&\frac{\partial}{\partial x_2}(d\frac{\partial u_j^i}{\partial x_2}) + \frac{\partial}{\partial x_3}(d\frac{\partial u_j^i}{\partial x_3}))dx_1 dx_2 dx_3 + \\
&\int_w^e \int_s^n \int_b^u u_j^{i-1} dx_1 dx_2 dx_3.
\end{aligned} \tag{16}$$

Let $clt(u_j^{i-1})(x) \equiv clt(u_j^{i-1})(P)$ for all $x \in \mathcal{V}$, i.e. we assume constant profile of this quantity in $\mathcal{V}$. Further, assume that diffusion fluxes are constant on each face of the volume $\mathcal{V}$. Then, applying the Green theorem to the first integral on the right hand side of (16) we obtain

$$\begin{aligned}
&\int_w^e \int_s^n \int_b^u u_j^i dx_1 dx_2 dx_3 = \\
&\tau clt(u_j^{i-1})(P) \quad h^2 \\
&(d(e)\frac{\partial u_j^i(e)}{\partial x_1} - d(w)\frac{\partial u_j^i(w)}{\partial x_1} + \\
&d(n)\frac{\partial u_j^i(n)}{\partial x_2} - d(s)\frac{\partial u_j^i(s)}{\partial x_2} + \\
&d(u)\frac{\partial u_j^i(u)}{\partial x_3} - d(b)\frac{\partial u_j^i(b)}{\partial x_3}) + \\
&\int_w^e \int_s^n \int_b^u u_j^{i-1} dx_1 dx_2 dx_3.
\end{aligned} \tag{17}$$

Approximating partial derivatives by central differences and approximating integrals using values at central points, we obtain the following difference equation holding in each grid point P

$$\begin{aligned}
&-a_W u_j^i(W) - a_S u_j^i(S) - a_B u_j^i(B) + \\
&+a_P u_j^i(P) - \\
&-a_E u_j^i(E) - a_N u_j^i(N) - a_U u_j^i(U) = b_P
\end{aligned} \tag{18}$$

where

$$\begin{aligned}
a_W &= \frac{\tau}{h^2} clt(u_j^{i-1})(P) g(|\nabla u_j^\sigma|)(w), \\
a_E &= \frac{\tau}{h^2} clt(u_j^{i-1})(P) g(|\nabla u_j^\sigma|)(e), \\
a_S &= \frac{\tau}{h^2} clt(u_j^{i-1})(P) g(|\nabla u_j^\sigma|)(s), \\
a_N &= \frac{\tau}{h^2} clt(u_j^{i-1})(P) g(|\nabla u_j^\sigma|)(n), \\
a_B &= \frac{\tau}{h^2} clt(u_j^{i-1})(P) g(|\nabla u_j^\sigma|)(b), \\
a_U &= \frac{\tau}{h^2} clt(u_j^{i-1})(P) g(|\nabla u_j^\sigma|)(u),
\end{aligned} \tag{19}$$

$$a_P = a_W + a_E + a_S + a_N + a_B + a_U + 1,$$
$$b_P = u_j^{i-1}(P).$$

Applying the zero Neumann boundary conditions we can represent the equations (18) in matrix form

$$\mathbf{A}\overline{u}_j^i = \overline{b} \tag{20}$$

where $\overline{u}_j^i$ represents the vector of unknown discrete values of u_j^i. The coefficients of the matrix $\mathbf{A}$ depend on u_j^σ and u_j^{i-1} and thus they are recomputed in each discrete frame and scale step. Because of the dependence on u_j^σ, we have to solve the equation (14). The finite volume method for (14) leads to a linear system represented by a symmetric matrix which is the same in each frame and scale step. Hence we obtain the values of u_j^σ in the grid points. Using those values we compute $g(|\nabla u_j^\sigma|)$ for each face central point. Finally we arrange the matrix $\mathbf{A}$ and we solve the system (20).

IV. Computational results

In this section we present and discuss the computational results obtained by the approximation scheme suggested in the previous section. First we consider a phantom-like image sequence consisting of an expanding, slightly deforming and translating ellipse with a four-petal structure inside. We add uniform noise to the image sequence. The original six-frame sequence and its noise-corrupted version are depicted in Figure 1. Figure 2 represents the results of the nonlinear multiscale analysis in the first, second and fifth discrete scale steps. We have used $\tau = 0.1$, $\sigma = 0.001$, $h = 1/64$.

Next we have applied multiscale analysis model to an in vivo acquired 3D echocardiographic sequence. The sequence has been obtained by means of a rotational acquisition technique using the TomTec Imaging System. With this technique the transducer undergoes a rotation around its main axis in a propeller configuration. A series of tomographies corresponding to the sections of a cone of biological tissue has been acquired. The acquisition consists of 14 image-cubes that represent a whole cardiac cycle of a real patient. A volume of interest of 150 x 150 x 100 voxels has been processed. The interval of time between one cube and the next one is 40 ms. In Figures 3–9 (first column) the left ventricular endocardium and the left atrium of an entire unfiltered cardiac cycle has been visualized. The quality of the 3D raw dataset is very good. Nevertheless a remarkable amount of noise is present in the sequence. The iso-surfaces corresponding to the interface between cardiac muscle and blood have been computed by the marching cubes method and visualized by a Gouraud shading surface rendering ([17], [31]). To clarify the visualization of the ventricular chambers we applied four cutting planes that isolate the region of interest. In clinical practice a cutting plane that filters out the "in front" regions is often used ([25]). The epicardium is not visible because the gray levels of his interface are out of the marching cubes threshold that we have chosen to visualize the left chambers. In particular the low echogenicity of the blood allows the choice of a low isosurface threshold that avoids the visualization of most of the other structures . Figures 3–9 consist of three sub-figures. For each row, in the left we plot the echo-volume visualized using the original noisy data, in the middle the result after three discrete scale steps and on the right after nine discrete scale steps. We have chosen $\tau = 0.2$, $\sigma = 0.0001$ and $h = 1/150$.

The parameter h represents the size of the pixel/voxel. In numerical integration of partial differential equations, a classical choice is to consider a rectangular domain with the longest side S of unitary length. In this case $h = 1/N_S$, where N_S is the number of equally spaced subintervals. In image processing N_S is naturally chosen as the number of pixels/voxels in the direction of the longest side.

For any choice of the scale step τ we have shown that the numerical scheme is unconditionally stable (see Appendix). However the low-order (first order) accuracy in the scale integration places a restriction on the maximum size of the scale step in order to be close to the continuous model (4). For practical purpose, we have obtained good results for a range of values [0.01,0.2].

The parameter σ in (14) corresponds to the shape of the Gauss function. Usually $\sigma < \tau$ where τ is the discrete scale step in (13). In the phantom sequence the structures to be preserved are quite large (more than 10 pixels) and we have used $\sigma = 0.001$. For the echo sequence we preserve spatial structures of small dimension by using $\sigma = 0.0001$.

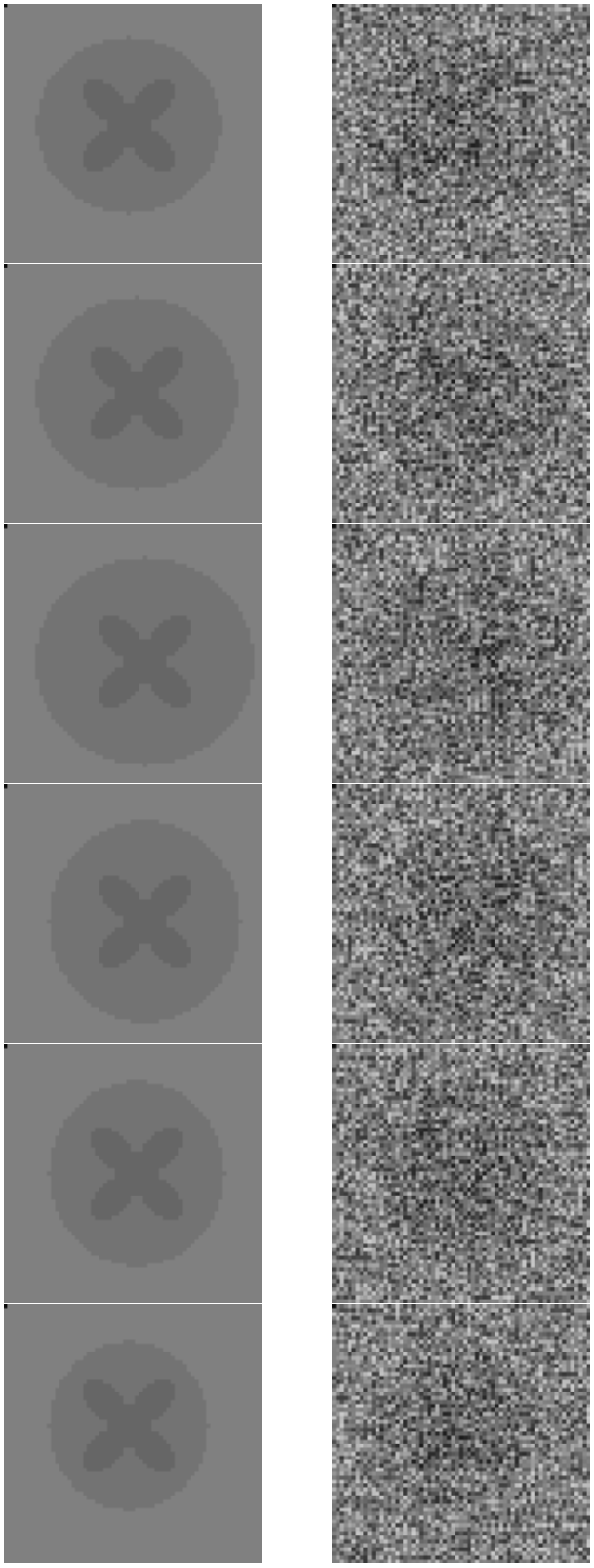

Fig. 1. 2D phantom - original and noisy images.

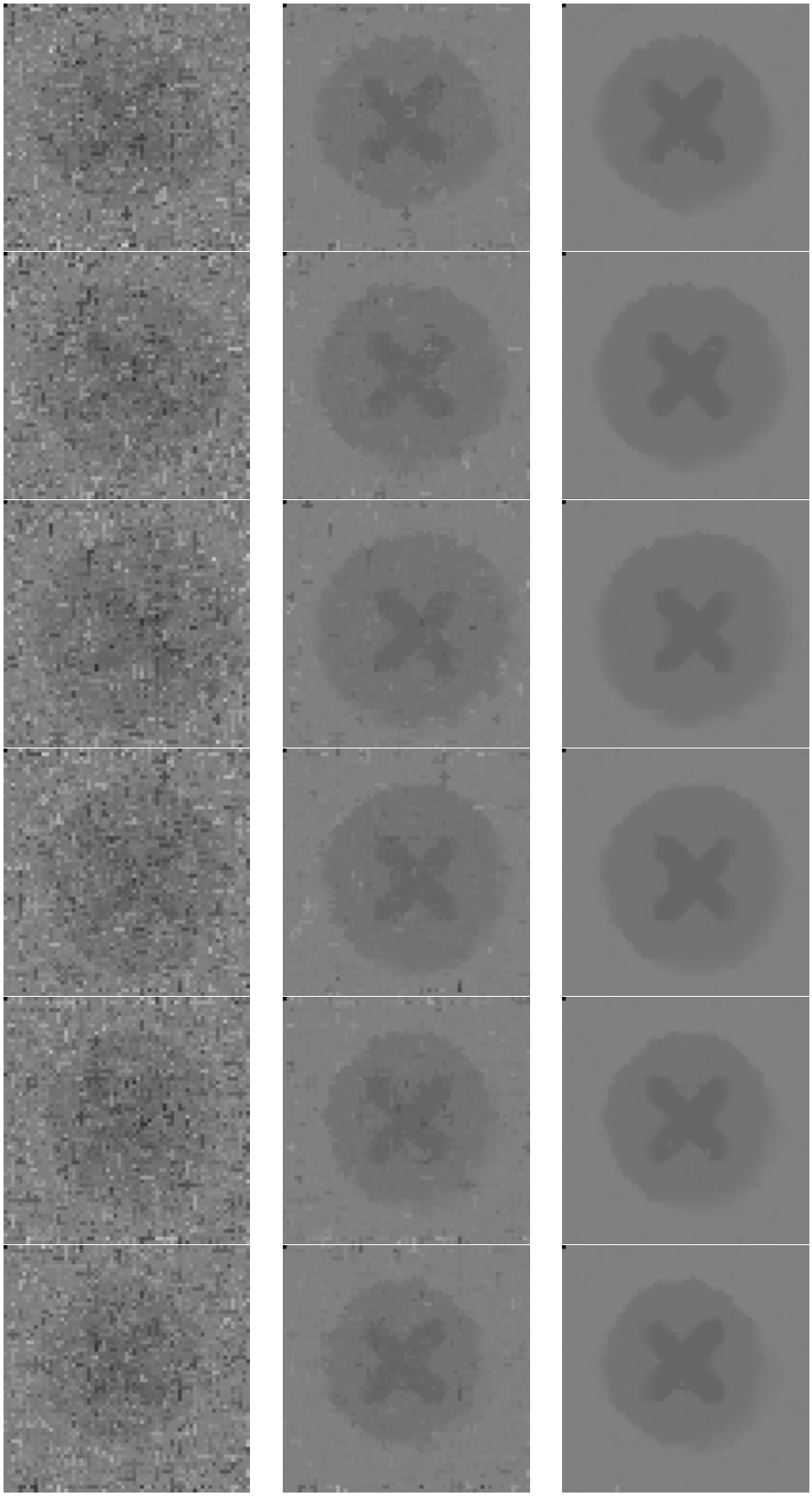

Fig. 2. 2D phantom - 1st, 2nd and 5th scale steps for each time frame.

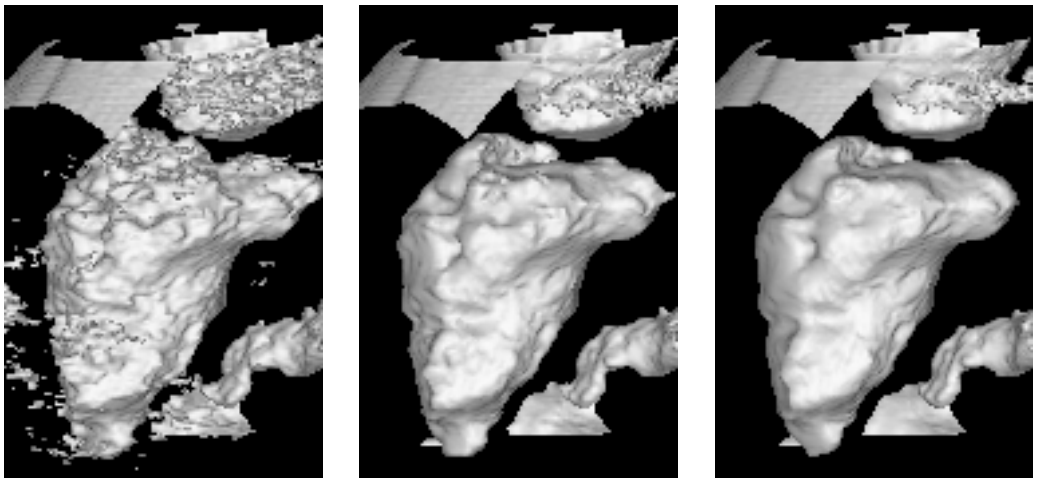

Fig. 3. Multiscale analysis of the 1st frame of the 3D echocardiographic sequence.

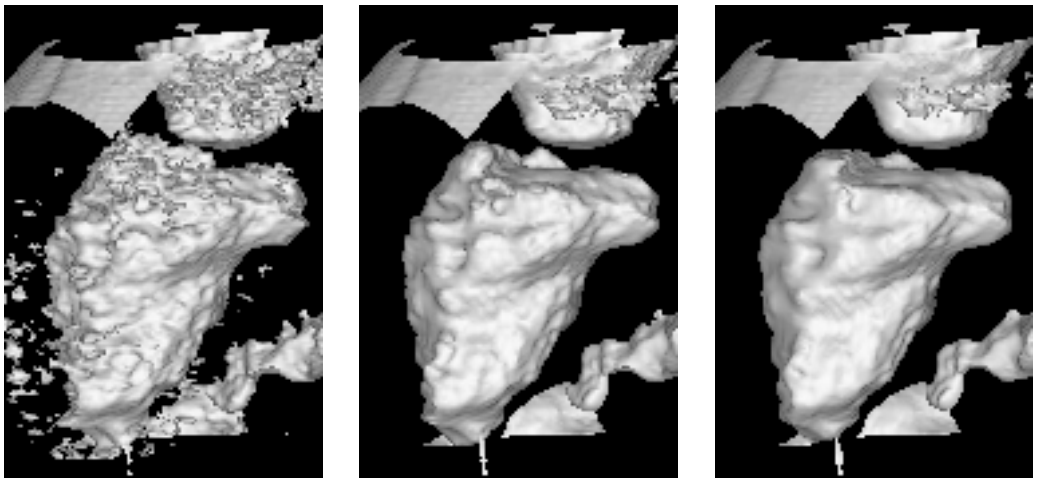

Fig. 4. Multiscale analysis of the 3rd frame of the 3D echocardiographic sequence.

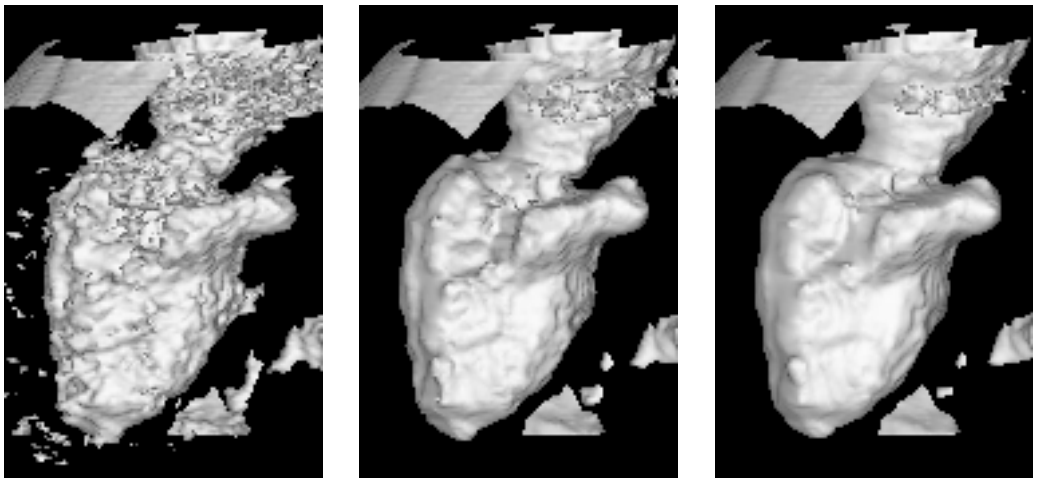

Fig. 5. Multiscale analysis of the 5th frame of the 3D echocardiographic sequence.

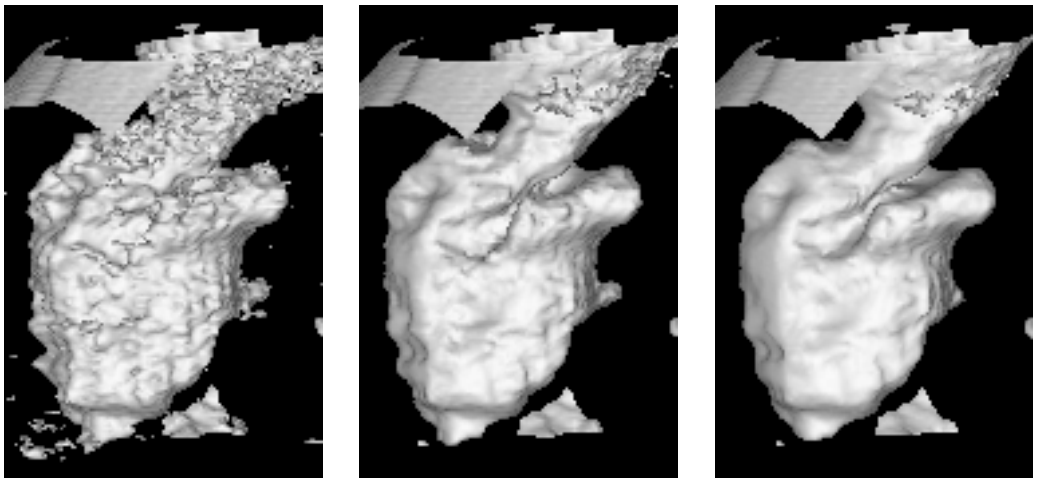

Fig. 6. Multiscale analysis of the 7th frame of the 3D echocardiographic sequence.

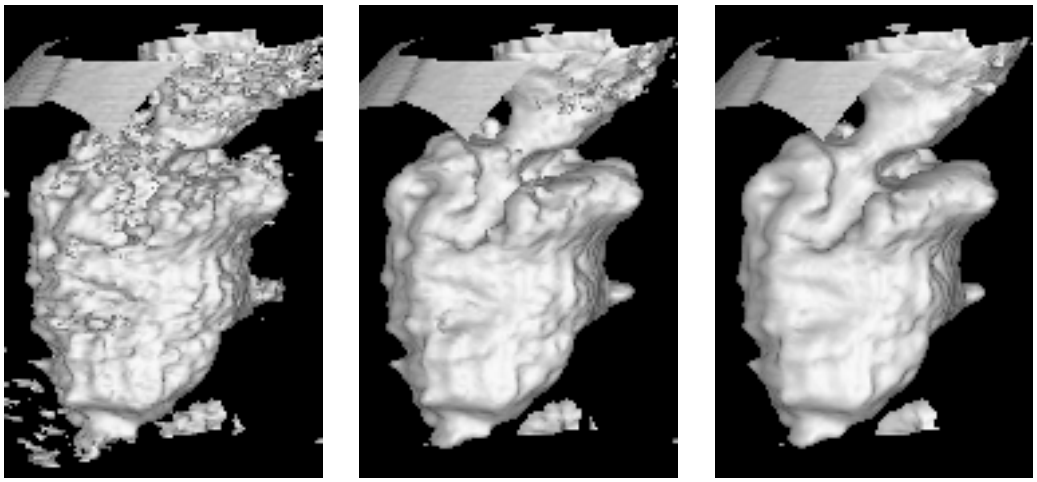

Fig. 7. Multiscale analysis of the 9th frame of the 3D echocardiographic sequence.

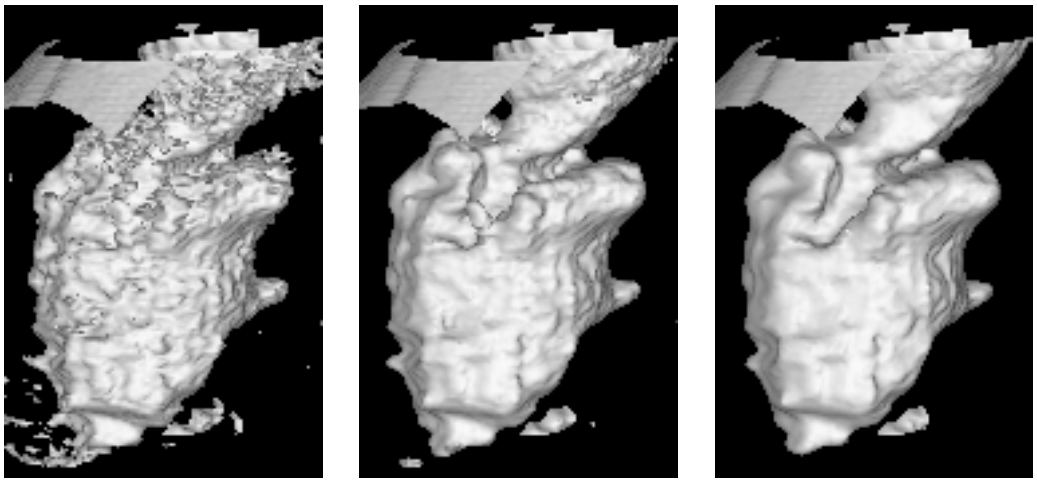

Fig. 8. Multiscale analysis of the 11th frame of the 3D echocardiographic sequence.

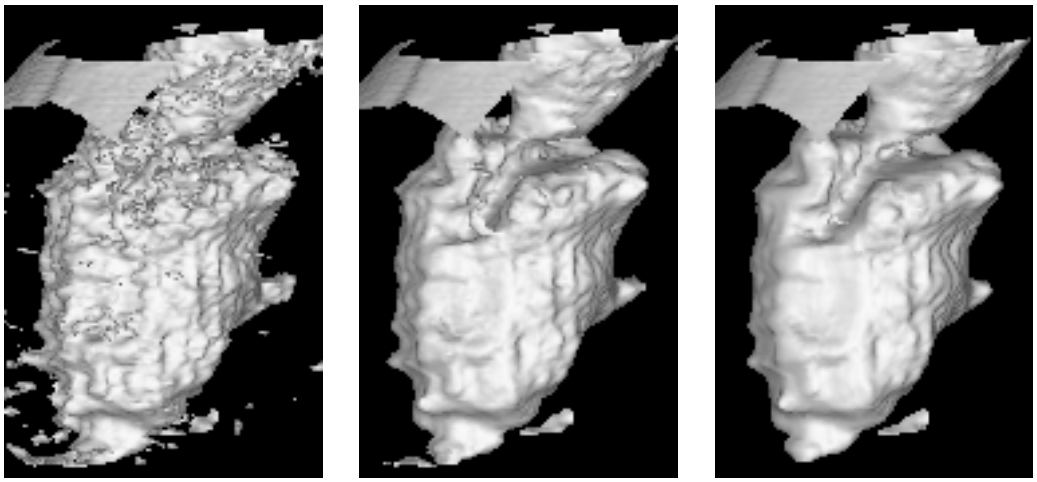

Fig. 9. Multiscale analysis of the 13th frame of the 3D echocardiographic sequence.

We want to evaluate the accuracy of the proposed multiscale analysis model. We are interested in noise removal by preserving the shape and the position of the coherent structures as much as possible. Thus we set the following procedure to define and estimate the error. An external observer has manually segmented the ventricular chamber by considering every single slice l of a 3D unfiltered frame. We compute the mean intensity value $\tilde{u}$ of the points corresponding to the manual segmentation over all the slices and we use $\tilde{u}$ to define the "closest" isosurface to the manual segmentation itself. In Figure 10 a slice of a 3D frame with the superimposition of $\tilde{u}$ iso-level curves is shown. In Figure 11 the same situation after 9 discrete scale steps is reproduced. The nonlinear multiscale analysis does not move significantly the position of the coherent boundaries as it is shown in Figure 12, where the contour lines of the unfiltered and filtered images are compared. At the same time the filtering of the non-coherent structures is performed. Our goal now is to estimate the mean distance between the manual segmentation and the isoline in both cases before and after filtering. For each slice a distance function $\mathcal{D}_l(x,y)$ from the isoline is computed with level set methods, following ([30]–Chapter 6). In Figure 13 the distance function from the isoline of Figure 12 is visualized. The mean distance between the manual segmentation curve C_l and the isoline is defined as $D_l = \int_{C_l} \mathcal{D}_l(x,y)ds / \int_{C_l} ds$, where s is the arclenght. In Figure 14 both C_l and $\mathcal{D}_l(x,y)$ are visualized. The distance error has been evaluated for every slice of the 3D dataset. The global distance error is computed by averaging the errors over the L slices, i.e. $D = \frac{1}{L}\sum_{l=1}^{L} D_l$. With this procedure we estimated $D = 1.3$ voxels for the unfiltered image and $D = 0.8$ voxels for the result of the multiscale analysis. Such results give a quantitative confirmation of the qualitative visual inspection, about the ability of the method to keep the position of the coherent structures.

V. Discussion

To fulfill the filtering requirements the echocardiographic sequence should be Lambertian and locally Galilean. The first requirement deals with the question: "Is the echographic signal a conservative quantity?". Experimental results show that the rotation and deformation of the tissue produce nonconservative effects of the brightness signal. It is therefore necessary to find out to what extent during the cardiac movement the brightness signal is conserved in the echocardiographic sequence. Let us consider the correlation between a deformed (rotated) reference echographic image and the echographic image obtained by deforming (rotating) the tissue in the same way. Meunier and Bertrand [21] developed a mathematical analysis which clearly shows how this correlation varies when a movement of translation, rotation and deformation is imposed on the tissue. This analysis has been applied to 3D echocardiographic sequences in [36]. The nonconservative phenomena have found to be negligible between subsequent frames and the brightness variation is due to a large extent to the transport alone of the muscular tissue. Such conclusions have been achieved in [21] and [36] also on the basis of the experimental results published by Streeter et al. ([32][33]). Moreover it should be observed that a number of approaches used for calculating the motion field from sequences of echocardiogra-

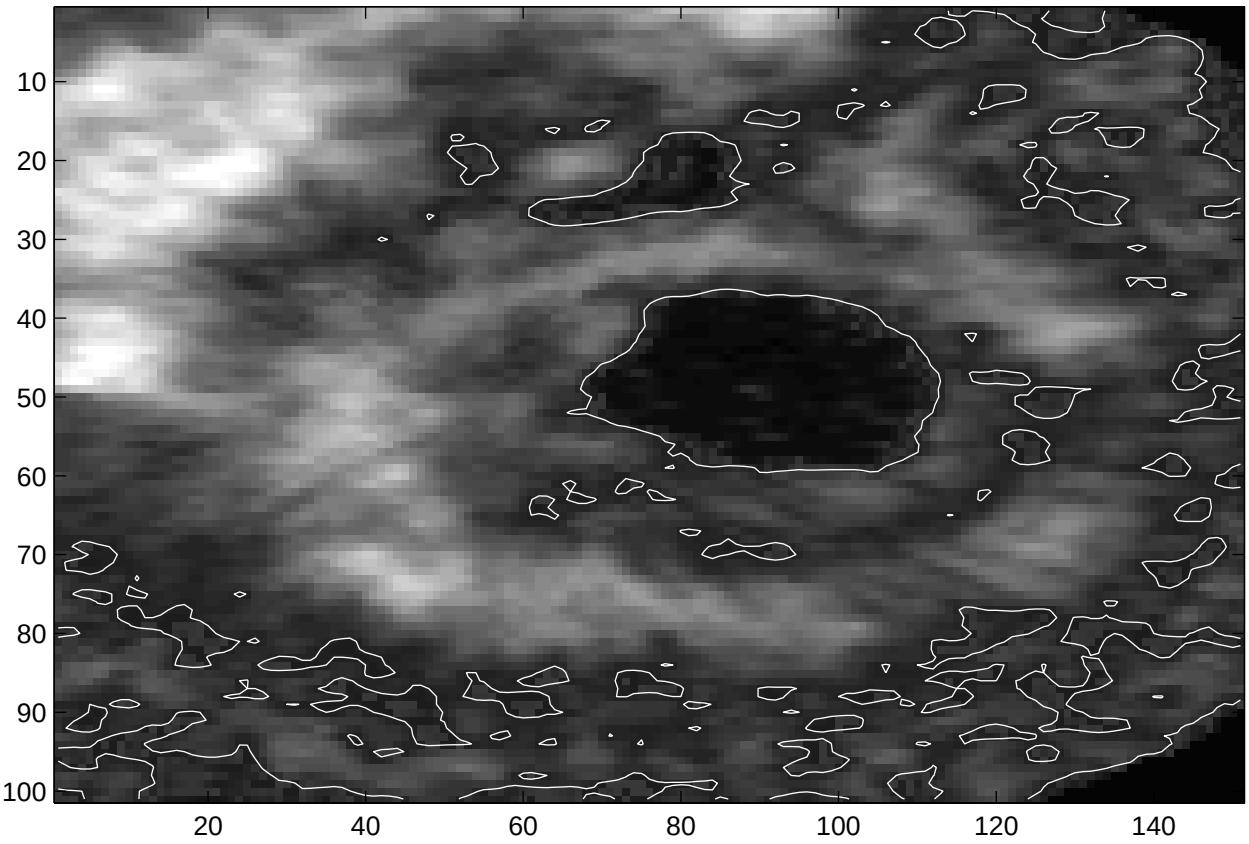

Fig. 10. The level contour line $u = \tilde{u}$ computed on the unfiltered slice y=103. The gray-level image is visualized in the background.

phies [18]-[20] implicitly assume that the variation of luminosity is due to the transport alone of the tissue, and thus, that the echocardiographic signal is a Lambertian quantity.

A motion is locally Galilean if the trajectory of each material point is smooth. In 3D echocardiographic sequences this is true for the two separate diastole and systole phases, while the motion is not Galilean during the change of phases where the acceleration is high and the motion tends to be non smooth. Nevertheless our experiments do not show a loss of accuracy in the edge preservation of this extremal points.

We finish the discussion by presenting several comparisons related to the efficiency of linear solvers for the linear system (20). The huge number of unknowns in each system and the sparsity pattern of the coefficient matrix suggest the use of an iterative solver. Research in iterative solvers is currently a very active field, see ([28]) and the quoted references. In our comparison we have chosen the classical and most relevant solvers, namely Gauss-Seidel method (GS), conjugate gradient method (CG), biconjugate gradient stabilized method (BICGSTAB), transpose free quasi minimal residual method (TFQMR), generalized minimum residual method (GMRES). With a good preconditioner, the total amount of steps required for convergence can be reduced dramatically, at the cost of a slight increase in the number of operations per step, resulting in much more efficient algorithms in general. In this first investigation we use for each method, when it is possible, the following well-known preconditioners: Right ILU(0) (zero fill-in incomplete LU factorization), Left ILU(0), Right MILU(0) (modified ILU(0)), Left MILU(0) and ILUT(n) (ILU with n-fill in and thresholding). For details we refer to ([28]) or ([9]). In case of GMRES method we allow the restart when the dimension of Krylov subspace is 20. We stop the iterations when the Euclidean norm of the actual residual $r^{(k)} = \overline{b} - \mathbf{A}\overline{u}_j^{i(k)}$ satisfies

$$\|r^{(k)}\| \leq \alpha \|r^{(0)}\|$$

with tolerance parameter $\alpha = 0.01$ and $r^{(0)}$ representing the initial residual. We start with $\overline{u}_j^{i(0)} = \overline{0}$.

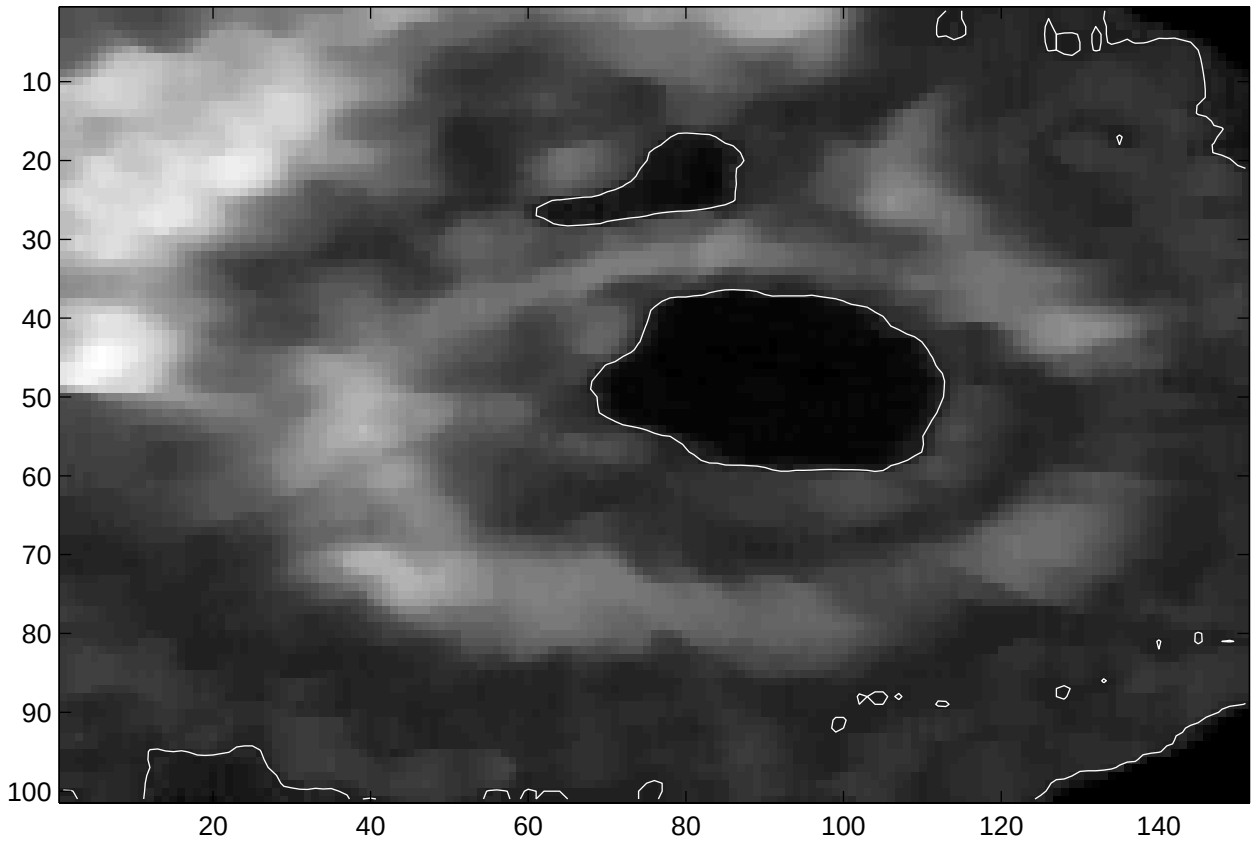

Fig. 11. The level contour line $u = \tilde{u}$ computed on the slice y=103 after 9 discrete scale steps of filtering. The filtered image is shown in the background.

We present two tables. Table 1 is related to computations on the first discrete scale level and Table 2 to computations on the third one. In the 2D testing example, we process a simple phantom given by a moving noisy circle and for report we choose the time frame from the middle of the sequence. We used $\tau = 0.1$, $\sigma = 0.001$ and $h = 1/128$. In the tables, we print the number of multiplications (matrix times vector) performed until convergence is reached because this is the most expensive step of the iterative procedure and this number is independent on computer architecture. We report also the CPU time in seconds (on SUN Sparc 10 workstation) for each complete iterative procedure. This comparison is related also to work ([35]) in which an additive operator splitting method (AOS) is used for solving the anisotropic diffusion equation by a semi-implicit technique. Such a method is direct and thus uses a fixed number of operations. They report that, in general, the AOS scheme is about three times faster than classical Gauss-Seidel method with the tolerance $\alpha = 0.01$. From our comparison, it is clear that any preconditioned iterative method is about 10 times faster than Gauss-Seidel procedure for matrices receiving from image multiscale analysis models. In the best case, using the GMRES method we have a speed-up of about 50. We conclude that semi-implicit numerical approximation leads to standard space discretization methods for boundary value problems and then to linear systems that can be solved efficiently by iterative solvers, even with the use of preconditioners designed for general classes of matrices. Clearly more investigations are necessary to design preconditioners for these specific matrices and underlying problem, and this will be a future research topic.

VI. Conclusions

The multiscale analysis of 3D echocardiographic sequences we proposed uses spatial and temporal information to filter out noise and to preserve the coherent space-time structures. The PDE representing the model combines the effect of the anisotropic diffusion in space and the movie multiscale analysis in time. In the limited number of synthesized and real sequences that we have considered the results are encouraging both

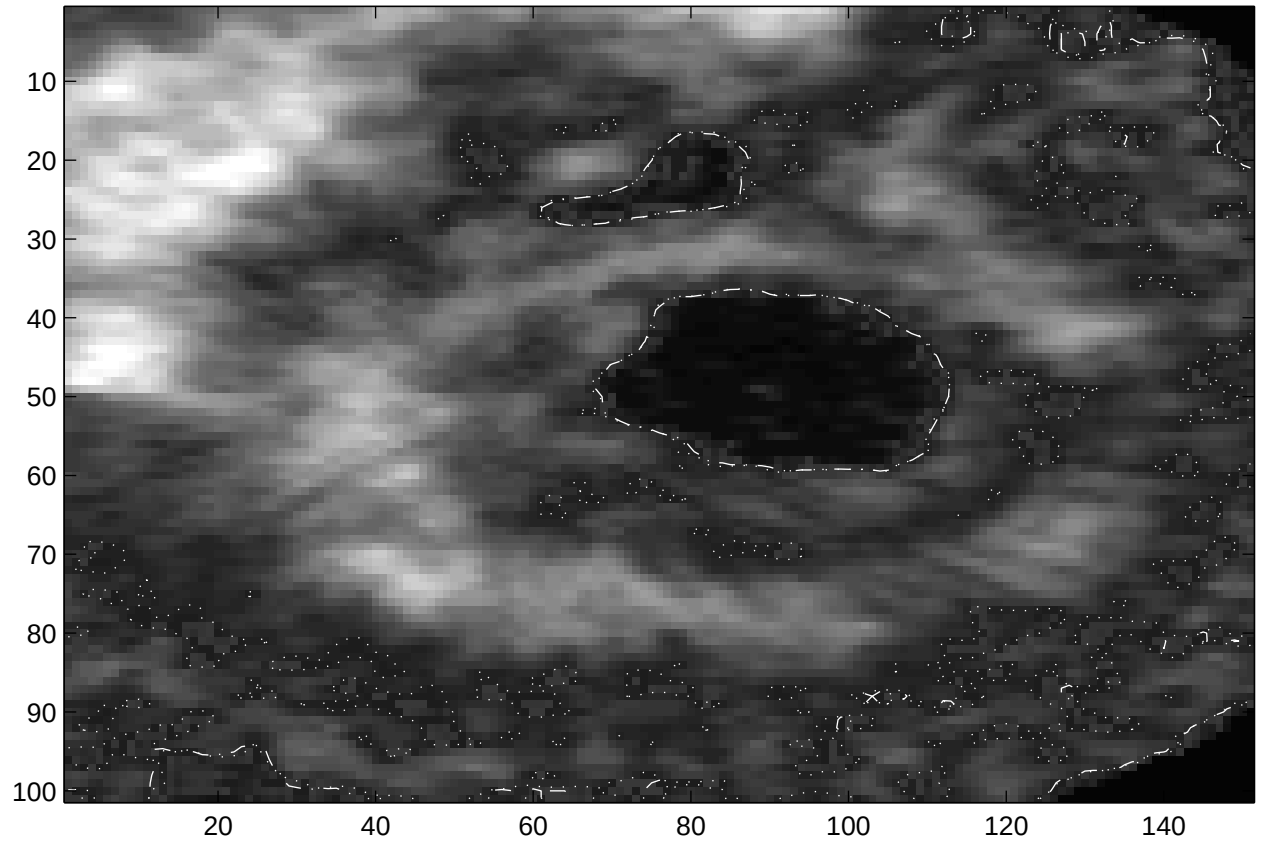

Fig. 12. Comparison between the contour lines corresponding to the unfiltered (dot) and filtered (dot-line) image. In background the unfiltered image is shown. For clarity of representation only the subregion around the left and right ventricles is visualized.

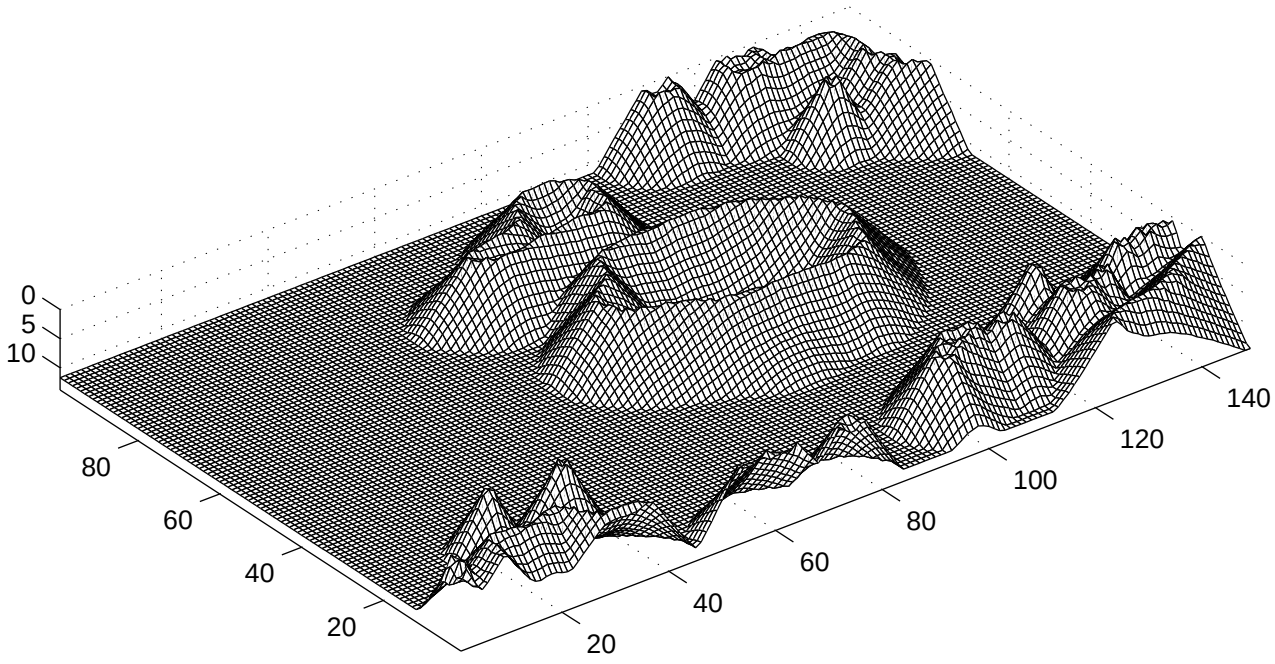

Fig. 13. Distance function $\mathcal{D}_l(x,y)$ from the $\tilde{u}$ level set of the filtered image (isoline of Figure 11). To allow a better visualization the elevation axis has been reversed (0 on the top) and the distance has been cuted off for $\mathcal{D}_l(x,y) > 10$.

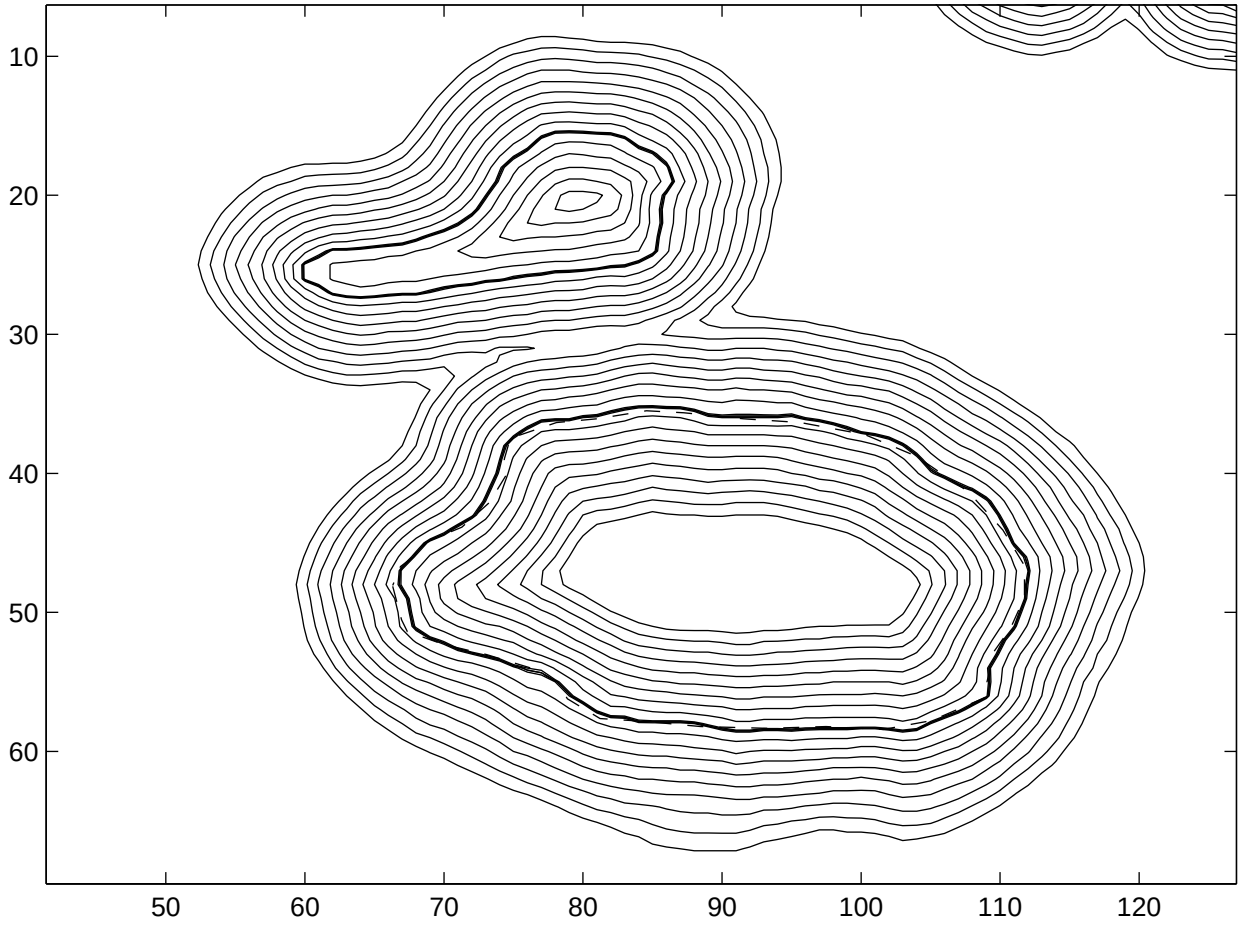

Fig. 14. The manual segmentation curve C_l (dashed line) over-imposed to the distance function $\mathcal{D}_l(x,y)$ (solid iso-contour lines). The thick lines represent the zero level set of $\mathcal{D}_l(x,y)$.

from the qualitative and quantitative point of view. In particular the boundaries of the coherent structures are not moved significantly while a remarkable reduction of the noise is provided. A statistically significant number of diagnostic cases has to be investigated to assess a full clinical validation. A robust numerical scheme to solve the discretized PDE has been proposed and a comparison among several iterative solvers has been performed. The method is efficient for 2D+time sequences while the 3D+time implementation is computationally intensive also due to the remarkable amount of data that has to be processed.

Acknowledgment. The numerical experiments presented in the paper were computed using large-scale computational facilities of the Supercomputing group at CINECA - InterUniversity Computing Center, Bologna (Italy). The authors are indebted to S.Bassini and G.Erbacci for their help in solving large scale problems. The author would like to thank Bernhard Mumm and TomTec, who have collected the sequence of 3D echo data. This work was supported by IPER ICARUS Project (funded by the European Commission - DGXII under the PECO program), CNR, Italy, and by Slovak national grant VEGA 1/3034/96. The work was supported in part by the Office of Energy Research, Office of Computational and Technology Research, Mathematical, Information and Computational Science Division, Applied Mathematical Sciences Subprogram, of the U.S. Department of Energy, under Contract No. DE-AC03-76SF00098.

References

[1] L. Alvarez, F. Guichard, P.L. Lions, J.M. Morel, *Axioms and Fundamental Equations of Image Processing*, Arch. Rat. Mech. Anal., vol.123, pp. 200-257 (1993)

[2] L. Alvarez, J.M. Morel, *Formalization and computational aspects of image analysis*, Acta Numerica, pp. 1-59 (1994)

[3] P. Baraldi, A. Sarti, C. Lamberti, A. Prandini, F. Sgallari, *Evaluation of differential optical flow techniques on synthesized echo images*, IEEE Trans. Biomedical Engineering, Vol 43, No. 3 (1996)

TABLE I

COMPARISON OF ITERATIVE SOLVERS (1ST SCALE STEP)

No.Multip/CPU time	GS	CG	BICGSTAB	TFQMR	GMRES
No Precon	265 / 25.39	94 / 6.25	98 / 7.14	204 / 17.72	114 / 19.28
Left ILU(0)		20 / 2.41	20 / 2.47	18 / 2.51	17 / 3.58
Right ILU(0)		No conver	16 / 2.03	16 / 2.32	7 / 1.13
Left ILU(0)		16 / 1.95	20 / 2.48	22 / 3.05	15 / 3.02
Right MILU(0)		5 / 0.69	20 / 2.46	12 / 1.72	5 / 0.8
ILUT(5)					3 / 0.51

TABLE II

COMPARISON OF ITERATIVE SOLVERS (3RD SCALE STEP)

No.Multip/CPU time	GS	CG	BICGSTAB	TFQMR	GMRES
No Precon	800 / 69.26	190 / 12.9	152 / 10.35	406 / 32.89	421 / 71.42
Left ILU(0)		No conver	54 / 6.05	54 / 6.76	41 / 8.74
Right ILU(0)		No conver	36 / 4.09	38 / 4.79	24 / 4.97
Left ILU(0)		43 / 4.60	44 / 4.85	52 / 6.42	32 / 6.38
Right MILU(0)		16 / 1.81	30 / 3.37	32 / 4.04	12 / 2.12
ILUT(5)					10 / 1.62

[4] E. Bänsch, K. Mikula, *A coarsening finite element strategy in image selective smoothing*, Computing and Visualization in Science, vol 1, pp. 53-61 (1997)

[5] W. Bommer, L. Weinert, A. Neumann, J. Neef, D. Mason, A. Demaria, *Determination of right atrial and right ventricular size by two-dimensional echocardiography*, Circulation, pp. 60-91 (1979)

[6] V. Caselles, C. Sbert, *What is the best causal scale space for three-dimensional images?* SIAM J. Appl. Math 56, pp. 1199-1246 (1996)

[7] M.G. Crandall, H. Ishii, P.L. Lions, *User's guide to viscosity solutions of second order partial differential equations*, Bull.(NS) Amer. Math. Soc., vol. 27, pp. 1-67 (1992)

[8] F. Catté, P.L. Lions, J.M. Morel, T. Coll, *Image selective smoothing and edge detection by nonlinear diffusion*, SIAM J. Numer. Anal., vol. 129, pp. 182-193 (1992)

[9] G. Golub, C. van Loan, *Matrix Computations (Third Edition)*, The Johns Hopkins Univ. Press (1996)

[10] F. Guichard, *Axiomatisation des analyses multi-échelles dímages et de films*, PhD Thesis Univerity Paris IX Dauphine (1994)

[11] A.Handlovičová, K.Mikula, A.Sarti, *Numerical solution of parabolic equations related to level set formulation of mean curvature flow*, Computing and Visualization in Science (1998)

[12] J. Kačur, K. Mikula, *Solution of nonlinear diffusion appearing in image smoothing and edge detection*, Applied Numerical Mathematics, vol. 17, pp. 47-59 (1995)

[13] J. Kačur, K. Mikula, *Slow and fast diffusion effects in image processing - Approximation schemes and numerical experiments.* Preprint IWR 96-26, University of Heidelberg (1996)

[14] J. Kačur, K. Mikula, *Slowed anisotropic diffusion*, in Scale-Space Theory in Computer Vision (ed. by B.t.H.Romeny, L.Florack, J.Koenderink, M.Viergever), Lecture Notes in Computer Science 1252, Springer pp. 357-360 (1997)

[15] C. Lamberti, F. Sgallari, *Edge detection and velocity field for the analysis of heart motion*, Digital Signal Processing 91, Elsevier (Editors V. Cappellini, A.G. Costantinides) pp. 603-608 (1991)

[16] P.L. Lions, *Axiomatic derivation of image processing models*, Math. Models Methods Appl. Sci., vol. 4, pp. 467-475 (1994)

[17] W.E. Lorensen, H.E. Cline *Marching cubes: a high resolution 3D surface construction algorithm*, Computer Graph., vol. 21, pp. 163-169 (1987)

[18] G.E.Maillaux, A.Bleau, M.Bertrand, R.Petitclerc, *Computer analysis of heart motion from two-dimensional echocardiograms*, IEEE Trans. Biomed. Eng., vol BME-34, pp. 356-364, 1987

[19] G.E.Maillaux, F.Laglois, P.Y.Simard, M.Bertrand, *Restoration of the velocity field of the heart from two-dimensional echocardiograms*, IEEE Trans. Med. Imag. vol. 8, pp. 143-153, 1989

[20] J.M.Meunier and M.Bertrand, *Tissue motion inferred from echocardiographic speckle tracking* in World Congress on Medical Physisc and Biomedical Engineering, Rio de Janeiro, p. 636, 1994

[21] J.M.Meunier and M.Bertrand, *Echographic image mean gray level changes with tissue dynamics: A system-based model study* IEEE Trans. Biomed. Eng., vol. BME-42, pp. 403-410, 1995.

[22] K. Mikula, A. Sarti, C. Lamberti, *Geometrical diffusion in 3D-echocardiography*, Proceedings of ALGORITMY'97 - Conference on Scientific Computing, West Tatra Mountains - Zuberec, pp. 167-181 (1997)
[23] S. Osher, J. Sethian, *Front propagating with curvature dependent speed: algorithms based on the Hamilton- Jacobi formulation*, J. Comput Phys. 78, 12-49
[24] S. Patankar, *Numerical heat transfer and fluid flow*, Hemisphere Publ. Comp. (1980)
[25] N.G. Pandian, J. Roelandt, N.C. Nanda, L. Sugeng, Q.L. Cao, J. Azevedo, S.L. Schwartz, M.A. Vannan, A. Ludomirski, G. Marx and M. Vogel, *Dynamic three-dimensional echocardiography: Methods and clinical potential*, Echocardiography, Vol. 11, No. 3, pp. 237-259, 1994
[26] P. Perona, J. Malik, *Scale space and edge detection using anisotropic diffusion*, In Proc. IEEE Computer Society Workshop on Computer Vision (1987)
[27] B.M.ter Haar Romeny (Ed.), *Geometry driven diffusion in computer vision*, Kluwer (1994)
[28] Y.Saad, *Iterative methods for sparse linear systems*, PWS Publ. Comp. (1996)
[29] J. Sethian, *Numerical algotithm for propagating interfaces: Hamilton-Jacobi equations and conservation laws*, J. Diff. Geom. 31 pp. 131-161 (1990)
[30] J. Sethian, *Level Set Methods. Evolving Interfaces in Geometry, Fluid Mechanics, Computer Vision, and Material Science*, Cambridge University Press (1996)
[31] W. Shroeder, K. Martin, B. Lorensen, *The visualization Toolkit*, Prentice Hall PTR., New Jersey (1996)
[32] D.D.Streeter and W.T.Hanna, *Engineering mechanics for successive states in canine left ventricular myocardium. II Fiber angle and sarcomere length*, Circ. Res. vol. 33, pp. 656-664, 1973.
[33] D.D.Streeter, *Fiber orientation in the canine left ventricle during diastole and systole*, Circ. Res. vol. 24, pp. 339-347, 1969.
[34] J. Weickert, *A review of nonlinear diffusion filtering*, in Scale-Space Theory in Computer Vision (ed. by B.t.H.Romeny, L.Florack, J.Koenderink, M.Viergever), Lecture Notes in Computer Science 1252, Springer pp. 3-28 (1997)
[35] J. Weickert, B.M.t.H. Romeny, M.A. Viergever, *Efficient and reliable schemes for nonlinear diffusion filtering*, to appear in IEEE Trans. on Image Processing (1998)
[36] G.Zini, A.Sarti, C.Lamberti *Application of continuum theory and multi-grid methods to motion evaluation from 3D Echocardiography*, IEEE Trans. Ultr. Ferr. Freq. Control, vol. 44, n.2, pp.297-308, 1997

VII. Appendix - Properties of the numerical approximation

In this Appendix, we prove that the numerical scheme proposed in the paper is unconditionally stable in the L_∞ sense.

The matrix $\mathbf{A}$ in (20) is non-symmetric but strictly diagonally dominant and thus invertible, so we can assert that the solution of the system (20) always exists and it can be expressed in the form

$$\overline{u}_j^i = \mathbf{B}\overline{u}_j^{i-1}, \text{ where } \mathbf{B} = \mathbf{A}^{-1}. \tag{21}$$

The coefficients of $\mathbf{A}$ fulfill

$$a_{kk} > 0, \forall k, \quad a_{kl} \leq 0, \forall k, l, k \neq l, \tag{22}$$

$$\sum_l a_{kl} = 1, \forall k. \tag{23}$$

Moreover, for the matrix $\mathbf{C} = \mathbf{I} - \mathbf{D^{-1}A}$, where $\mathbf{D}$ is the diagonal of $\mathbf{A}$, we have

$$\rho(\mathbf{C}) \leq \|\mathbf{C}\|_\infty = \max_k \sum_l |c_{kl}| < 1. \tag{24}$$

Thus, using e.g. ([28], Theorem 1.16) we have that $\mathbf{A}$ is a M-matrix and hence for its inverse $\mathbf{B}$ we obtain

$$b_{kl} \geq 0, \forall k, l. \tag{25}$$

Using (23) we have that $\mathbf{A}\overline{v} = \overline{v}$ for $\overline{v} = (1, 1, ..., 1)$ and hence $\mathbf{B}\overline{v} = \mathbf{BA}\overline{v} = \overline{v}$ from which

$$\sum_l b_{kl} = 1, \forall k \tag{26}$$

holds, too. Now let

$$\min = \inf \overline{u}_j^{i-1}(k)$$

and

$$\max = \sup \overline{u}_j^{i-1}(k)$$

where by $\overline{u}_j^{i-1}(k)$ we denote the k-th component of the vector $\overline{u}_j^{i-1}$. Then due to (25) and (26) we have

$$\min = \sum_l b_{kl} \min \leq \sum_l b_{kl} \overline{u}_j^{i-1}(l) = \overline{u}_j^i(k), \forall k$$
$$\overline{u}_j^i(k) = \sum_l b_{kl} \overline{u}_j^{i-1}(l) \leq \sum_l b_{kl} \max = \max, \forall k.$$

Thus, the so called L_∞-stability condition is fulfilled for the discrete solution.in each discrete frame and scale step. Let a, b be real constants. We can state the following stability result:

$$\begin{array}{lll} \text{If} & a \leq \overline{u}_j^0 \leq b, & j = 0, ..., m \\ \text{then} & a \leq \overline{u}_j^i \leq b, & \forall j = 0, ..., m, \quad i = 1, 2, ... \end{array}$$

which means that L_∞-stability condition holds for the entire discrete multiscale image sequence.